

# Precisely loading Pt on Tb<sub>4</sub>O<sub>7</sub>/CN heterojunction for efficient photocatalytic overall water splitting: Design and mechanism

Dedong Zeng, Yuexiang Li \*

School of Chemistry and Chemical Engineering, Key Laboratory of Jiangxi Province for Environment and Energy Catalysis, Nanchang University, Nanchang 330031, PR China



## ARTICLE INFO

### Keywords:

Photocatalytic overall water splitting  
Tb<sub>4</sub>O<sub>7</sub>/CN  
Pt loading site  
Synergistic effect  
Anti-synergistic effect

## ABSTRACT

Constructing heterojunction is an effective strategy for fighting electron-hole pairs recombination. Loading of hydrogen evolution reaction (HER) cocatalysts on a heterojunction is crucial for efficient photocatalytic overall water splitting (POWS). However, how to achieve a synergy between the heterojunction and HER cocatalyst remains a challenge. Herein, we propose a novel design strategy: selectively loading HER cocatalyst Pt on Tb<sub>4</sub>O<sub>7</sub>/CN. We found that engineering Pt on the Tb<sub>4</sub>O<sub>7</sub> section of Tb<sub>4</sub>O<sub>7</sub>/CN can synergistically promote the photogenerated charge separation and thus enhances the POWS activity. The H<sub>2</sub> production rate is about 2.8 times higher than that of Tb<sub>4</sub>O<sub>7</sub>/CN. In contrast, engineering Pt on the CN section leads to increasing photogenerated electron-hole recombination and deactivating the POWS activity, about 2.6 times as low as that of Tb<sub>4</sub>O<sub>7</sub>/CN. These findings highlight the significance of synergism of Pt loading sites with the charge separation of heterojunctions, providing insights on developing efficient photocatalysts for POWS.

## 1. Introduction

POWS is a promising approach for addressing energy shortage and environmental issues by converting inexhaustible solar energy into green H<sub>2</sub> fuel and high-value H<sub>2</sub>O<sub>2</sub> [1–9]. Carbon nitride (CN) as a metal-free semiconductor has attracted considerable attention for its potential application in POWS since Wang and his coworkers developed it as a photocatalyst in 2009 [10–16]. However, multiple developed CN-based photocatalysts cannot satisfy the requirement of the large-scale practical application because of the fast electron-hole pairs recombination and the sluggish HER reaction kinetics [17–19]. The strategies for improving charge separation include morphology engineering [20,21], cocatalyst incorporation [22–25] and heterojunction construction [26–33] etc. Among them, heterojunction construction is the most effective approach for accelerating the separation/transmission of photogenerated electron-hole pairs [28,29], including Z-scheme heterojunction [34], S-scheme heterojunction [35,36] and anisotropic heterojunction [27,28] etc. Although many heterojunctions have been reported, there are few reports on CN-based heterojunctions decorated by rare earth oxides [30,31].

Recently, Tb<sub>4</sub>O<sub>7</sub>/CN heterojunction with a distinctive sandwich structure has been successfully explored [32]. The introduced Tb<sub>4</sub>O<sub>7</sub>

remarkably enhances the charge separation in Tb<sub>4</sub>O<sub>7</sub>/CN heterojunction and acts simultaneously as a HER cocatalyst. However, the HER activity of Tb<sub>4</sub>O<sub>7</sub> is limited. Loading an efficient HER cocatalyst is expected. Pt is a highly efficient HER cocatalyst that has been widely used for improving the POWS performance of heterojunctions [37–39]. Because Tb<sub>4</sub>O<sub>7</sub>/CN heterojunction has realized considerable charge separation, the Pt loading sites should be compatible with the separation and transport of photogenerated charges. Thus, unveiling the nature of the synergistic effect of the Pt loading sites is a key issue to be solved [40]. Besides, the precise loading of Pt on a given location of the heterojunction also faces a great challenge [41,42].

In this study, precisely loading metallic Pt on Tb<sub>4</sub>O<sub>7</sub>/CN heterojunction has been achieved by a controllable photo-deposition strategy through engineering surface charge of Tb<sub>4</sub>O<sub>7</sub>/CN heterojunction and employing two charged precursors of Pt: [PtCl<sub>6</sub>]<sup>2-</sup> and [Pt(NH<sub>3</sub>)<sub>4</sub>]<sup>2+</sup>. As the negative-charged [PtCl<sub>6</sub>]<sup>2-</sup> is adopted, Pt is selectively loaded on the positive-charged Tb<sub>4</sub>O<sub>7</sub> section of Tb<sub>4</sub>O<sub>7</sub>/CN heterojunction to form Pt-Tb<sub>4</sub>O<sub>7</sub>/CN photocatalyst. The Pt loading in this mode is synergistic with the charge separation of Tb<sub>4</sub>O<sub>7</sub>/CN. On the other hand, when [Pt(NH<sub>3</sub>)<sub>4</sub>]<sup>2+</sup> is employed, the metallic Pt is selectively loaded on CN of Tb<sub>4</sub>O<sub>7</sub>/CN heterojunction to construct Tb<sub>4</sub>O<sub>7</sub>/CN-Pt heterojunction photocatalyst, which is anti-synergistic with the charge separation.

\* Corresponding author.

E-mail address: liyx@ncu.edu.cn (Y. Li).

Under the synergistic case, Pt-Tb<sub>4</sub>O<sub>7</sub>/CN displays a great enhancement of POWS activity with a H<sub>2</sub> evolution rate of 132 μmol h<sup>-1</sup> g<sup>-1</sup>, accompanying with stoichiometric H<sub>2</sub>O<sub>2</sub> production, which is about 2.8 times as high as that of Tb<sub>4</sub>O<sub>7</sub>/CN heterojunction. The apparent quantum yield (AQY) for H<sub>2</sub> evolution at 420 nm reaches to 5.9%. However, under the anti-synergistic case, the H<sub>2</sub> evolution rate and H<sub>2</sub>O<sub>2</sub> production rate of Tb<sub>4</sub>O<sub>7</sub>/CN-Pt photocatalyst are 18.2 and 16.5 μmol h<sup>-1</sup> g<sup>-1</sup>, respectively, about 2.6 times as low as that of Tb<sub>4</sub>O<sub>7</sub>/CN heterojunction. These findings highlight the significance of the synergism of Pt loading sites with charge carrier separation/transfer of heterojunctions, providing insights on developing efficient heterojunction photocatalysts for POWS by manipulating electron/hole transfer kinetics.

## 2. Experimental

### 2.1. Preparation of Tb<sub>4</sub>O<sub>7</sub>/CN heterojunction photocatalyst

Tb<sub>4</sub>O<sub>7</sub>/CN heterojunction was synthesized according to our previous work [32]. Firstly, 10.0 g of melamine and 37.5 mg of Tb<sub>4</sub>O<sub>7</sub> were mixed in an agate mortar. Secondly, the mixed powder was spread uniformly on a cylindrical alumina crucible with a lid and heated at a rate of 5 °C min<sup>-1</sup> to 520 °C and hold the temperature for 2 h. After cooling to room temperature, the final Tb<sub>4</sub>O<sub>7</sub>/CN heterojunction was obtained by grinding. For comparison, pristine CN was prepared via the similar method for Tb<sub>4</sub>O<sub>7</sub>/CN heterojunction in the absence of Tb<sub>4</sub>O<sub>7</sub>.

### 2.2. Zeta potential determination of Tb<sub>4</sub>O<sub>7</sub> and CN

Similar to the previous reports, the Zeta potentials of pristine CN [43] and bare Tb<sub>4</sub>O<sub>7</sub> [44] were measured in phosphate buffered solutions (PBS) on a Zeta potential analyzer (Malvern, Zetasizer Nano, ZS90). In brief, 5.0 mg of the as-prepared CN sample was decentralized in 5.0 mL of a PBS followed by ultrasonication treatment for 30 min. Subsequently, the resultant suspension was transferred to a test cell of the apparatus to read the zeta potential values. Each specimen was tested three times to take the average value. The pH value (3.5, 4.5, 5.5, 6.8, or 7.8) of the PBS was obtained by mixing different volumes of 0.20 M K<sub>2</sub>HPO<sub>4</sub>, KH<sub>2</sub>PO<sub>4</sub> and KH<sub>2</sub>PO<sub>4</sub> solution with the assistance of a pH device. The isoelectric point (IEP) was determined by plotting the zeta potential against the pH value. The IEP of Tb<sub>4</sub>O<sub>7</sub> was similarly obtained.

### 2.3. Preparation of Pt-Tb<sub>4</sub>O<sub>7</sub>/CN-x photocatalysts

Pt-Tb<sub>4</sub>O<sub>7</sub>/CN-x photocatalysts were prepared by a photo-deposition method using the as-prepared Tb<sub>4</sub>O<sub>7</sub>/CN heterojunction as the raw material and H<sub>2</sub>PtCl<sub>6</sub> as the Pt source. Firstly, 100.0 mg of Tb<sub>4</sub>O<sub>7</sub>/CN heterojunction was added into 100.0 mL of a PBS with a certain pH value (4.5, 5.7, 6.8, 7.8, 9.0 or 10) under vigorous stirring, and subsequently, 0.8 mL of H<sub>2</sub>PtCl<sub>6</sub> solution (1.93 × 10<sup>-3</sup> mol/L) was added dropwise into the suspension. Then, the suspension was poured into a quartz reactor followed by vacuum treatment to degas the air. And then, the suspension was irradiated with a Xe lamp for 2 h under magnetic stirring. During the process, the [PtCl<sub>6</sub>]<sup>2-</sup> was photo-reduced into metallic Pt. Finally, the solid product was separated by centrifugation, washed times with deionized (DI) water, and dried at 60 °C in a vacuum oven overnight. The obtained sample was labeled as Pt-Tb<sub>4</sub>O<sub>7</sub>/CN-x, where x represented the pH value of the PBS. When pH was 7.8, Pt was selectively loaded on the Tb<sub>4</sub>O<sub>7</sub> section of Tb<sub>4</sub>O<sub>7</sub>/CN. Consequently, the name of Pt-Tb<sub>4</sub>O<sub>7</sub>/CN-7.8 was simplified as Pt-Tb<sub>4</sub>O<sub>7</sub>/CN.

### 2.4. Preparation of Tb<sub>4</sub>O<sub>7</sub>/CN-Pt photocatalyst

Tb<sub>4</sub>O<sub>7</sub>/CN-Pt, in which Pt was selectively loaded on the CN section of Tb<sub>4</sub>O<sub>7</sub>/CN, was prepared by a similar photo-deposition method using [Pt(NH<sub>3</sub>)<sub>4</sub>]Cl<sub>2</sub> as the Pt source. In brief, 100.0 mg of Tb<sub>4</sub>O<sub>7</sub>/CN heterojunction was added into 100.0 mL of pH 7.8 PBS followed by vigorous

stirring, and subsequently, 0.78 mL of [Pt(NH<sub>3</sub>)<sub>4</sub>]Cl<sub>2</sub> (2.0 × 10<sup>-3</sup> mol/L) was added dropwise into the suspension. Then, this suspension was transferred into a vacuum quartz reactor. And then, the [Pt(NH<sub>3</sub>)<sub>4</sub>]<sup>2+</sup> was photo-reduced into metallic Pt with the assistance of the Xe lamp irradiation for 2 h. Finally, the solid product was separated by centrifugation, washed times with DI water, and dried at 60 °C in a vacuum oven overnight to obtain the Tb<sub>4</sub>O<sub>7</sub>/CN-Pt photocatalyst.

### 2.5. Photocatalytic overall water splitting performance

The POWS reaction was implemented in a vacuum quartz reactor linked to a N<sub>2</sub> gas-circulation equipment (Labsolar 6 A, Beijing Perfectlight). 50.0 mg of the as-prepared photocatalyst was dispersed in 100.0 mL of DI water. A 300 W Xe lamp (TSL-300S, Jiangsu Hengxi New Material Technology Co., Ltd) was employed as the light resource with a 420 nm optical filter to ensure visible light irradiation ( $\lambda > 420$  nm). Before the POWS reaction, the reaction system was evacuated to remove the air thoroughly. During the POWS process (8 h), magnetic stirring was applied to keep the powder photocatalyst in a suspension state, and the circulated cooling water was employed to maintain the temperature of the reaction system at 6 °C. The gas product (H<sub>2</sub>) was monitored at a given interval (one hour) on an online gas chromatograph (GC) (thermal conductivity detector, X13-molecular sieve column, nitrogen as carried gas). The liquid product (H<sub>2</sub>O<sub>2</sub>) was tested by UV-Vis spectrophotometry (UV6100) at 530 nm wavelength with a titanium sulfate as the chromogenic agent [45]. The stability of Pt-Tb<sub>4</sub>O<sub>7</sub>/CN for POWS was operated for 5 successive cycles. In each cycle, the photocatalyst was separated by centrifugation. The recovered photocatalyst was re-decentralized in 100.0 mL DI water, followed by deaeration and subsequently 4 h light radiation for a new cycle.

The raw materials, the specimen characterizations, the AQY determination of optical reaction and photo-electrochemistry measurements are detailed in the supporting information.

## 3. Results and discussion

### 3.1. Orient loading of Pt on Tb<sub>4</sub>O<sub>7</sub> of Tb<sub>4</sub>O<sub>7</sub>/CN and its effect on POWS

#### 3.1.1. Design, preparation and characterization

The prepared Tb<sub>4</sub>O<sub>7</sub>/CN heterojunction is used as raw material for loading Pt. The Fourier transform infrared (FT-IR) spectrum (Fig. S1a) and X-ray diffraction (XRD) pattern (Fig. S1b) of Tb<sub>4</sub>O<sub>7</sub>/CN heterojunction reveal that the prepared Tb<sub>4</sub>O<sub>7</sub>/CN is a composite of Tb<sub>4</sub>O<sub>7</sub> and CN. The scanning electron microscope (SEM) image (Fig. S2) shows a distinctive sandwich structure of Tb<sub>4</sub>O<sub>7</sub>/CN heterojunction.

In this work, oriented loading of Pt on Tb<sub>4</sub>O<sub>7</sub>/CN is realized by engineering surface charge and photo-reduction technique. To achieve precise loading of metallic Pt on the Tb<sub>4</sub>O<sub>7</sub> section of Tb<sub>4</sub>O<sub>7</sub>/CN using [PtCl<sub>6</sub>]<sup>2-</sup> as the precursor, the IEPs of CN and Tb<sub>4</sub>O<sub>7</sub> were determined by measuring the Zeta potential at a series of pHs. Fig. S3 shows that the IEP values of CN and Tb<sub>4</sub>O<sub>7</sub> are 5.6 and 9.5, respectively. The result means that when the Tb<sub>4</sub>O<sub>7</sub>/CN heterojunction is placed into a PBS reaction solution with a pH < 5.6, both Tb<sub>4</sub>O<sub>7</sub> and CN are positively charged, which can attract the [PtCl<sub>6</sub>]<sup>2-</sup>. However, when the pH of the reaction solution is in the range of 5.6–9.5, [PtCl<sub>6</sub>]<sup>2-</sup> cannot be adsorbed on the CN section of Tb<sub>4</sub>O<sub>7</sub>/CN due to electrostatic repulsion, but can be adsorbed on the Tb<sub>4</sub>O<sub>7</sub> section of Tb<sub>4</sub>O<sub>7</sub>/CN owing to the electrostatic attraction. Thus, as is shown in Fig. 1, when Tb<sub>4</sub>O<sub>7</sub>/CN is irradiated by visible light at pH 7.8, [PtCl<sub>6</sub>]<sup>2-</sup> can be reduced into metallic Pt on the Tb<sub>4</sub>O<sub>7</sub> section of Tb<sub>4</sub>O<sub>7</sub>/CN by the photogenerated electrons from Tb<sub>4</sub>O<sub>7</sub>/CN. However, at pH 4.5, metallic Pt is deposited in both CN and Tb<sub>4</sub>O<sub>7</sub> sections of Tb<sub>4</sub>O<sub>7</sub>/CN due to the non-selective adsorption of [PtCl<sub>6</sub>]<sup>2-</sup>.

The FT-IR spectra (Fig. S4a), XRD patterns (Fig. S4b), SEM images (Fig. S5a-b) and BET analysis (Fig. S6a-b) of Pt-Tb<sub>4</sub>O<sub>7</sub>/CN-4.5 and Pt-Tb<sub>4</sub>O<sub>7</sub>/CN evidently demonstrate that the loading Pt does not alter the

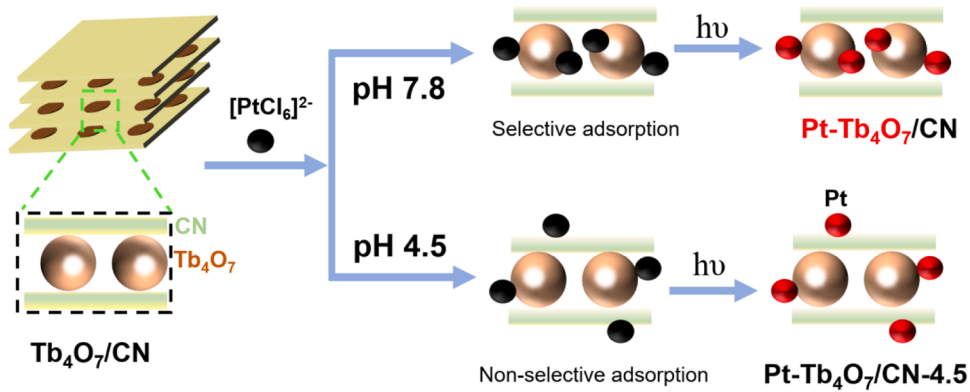


**Fig. 1.** Schematic diagram of the preparation process of Pt-Tb<sub>4</sub>O<sub>7</sub>/CN and Pt-Tb<sub>4</sub>O<sub>7</sub>/CN-4.5 photocatalysts.

composition and distinctive sandwich structure of Tb<sub>4</sub>O<sub>7</sub>/CN heterojunction (Fig. S2). The inductively coupled plasma atomic emission spectrometer (ICP-AES) (Fig. S7) analysis confirms that the Pt has been successfully loaded on Pt-Tb<sub>4</sub>O<sub>7</sub>/CN-4.5 and Pt-Tb<sub>4</sub>O<sub>7</sub>/CN, and their loading amounts are close. The transmission microscope (TEM) (Fig. 2a<sub>1</sub>) shows that the loading of Pt on Pt-Tb<sub>4</sub>O<sub>7</sub>/CN is uneven, while the loading Pt on Pt-Tb<sub>4</sub>O<sub>7</sub>/CN-4.5 is relatively even (Fig. 2b<sub>1</sub>). The High-Resolution TEM (HRTEM) image of Pt-Tb<sub>4</sub>O<sub>7</sub>/CN (Fig. 2a<sub>2</sub>) confirms that a Pt particle (red circle) is loaded on the Tb<sub>4</sub>O<sub>7</sub> section of Tb<sub>4</sub>O<sub>7</sub>/CN because the lattice fringe spaces of 0.23 nm and 0.30 nm relate to the (111) crystal facet of metallic Pt [39] and (111) crystal facet of Tb<sub>4</sub>O<sub>7</sub>, respectively. On the other hand, the HRTEM image of Pt-Tb<sub>4</sub>O<sub>7</sub>/CN shows that there is no Pt particle in the amorphous CN area (Fig. 2a<sub>3</sub>). These results clearly demonstrate that the Pt loading of Pt-Tb<sub>4</sub>O<sub>7</sub>/CN is oriented to Tb<sub>4</sub>O<sub>7</sub>. However, for Pt-Tb<sub>4</sub>O<sub>7</sub>/CN-4.5 photocatalyst, the loading of Pt is non-selective. It can be ascribed to the fact that the lattice fringe of Pt can be discovered not only on Tb<sub>4</sub>O<sub>7</sub>

(Fig. 2b<sub>2</sub>) but also on an amorphous CN (Fig. 2b<sub>3</sub>). The High-Resolution X-ray photoelectron spectra (HR-XPS) of Pt 4 f (Fig. 2c) further confirm that the Pt deposited in Pt-Tb<sub>4</sub>O<sub>7</sub>/CN and Pt-Tb<sub>4</sub>O<sub>7</sub>/CN-4.5 are metallic Pt due to the characteristic double peaks of 74.7/74.5 and 71.6/71.4 eV which are ascribed to Pt 4 f<sub>5/2</sub> and 4 f<sub>3/2</sub>, respectively [46]. Compared to that of Pt-Tb<sub>4</sub>O<sub>7</sub>/CN, the Pt 4 f binding energy of Pt-Tb<sub>4</sub>O<sub>7</sub>/CN-4.5 decreases by 0.2 eV, indicating that an interaction between metallic Pt and N of CN occurs in Pt-Tb<sub>4</sub>O<sub>7</sub>/CN-4.5 due to the Lewis acid-base coordination but not in Pt-Tb<sub>4</sub>O<sub>7</sub>/CN [47]. Fig. 2d exhibits the HR-XPS spectra of N 1 s, the binding energy peaks of Tb<sub>4</sub>O<sub>7</sub>/CN located at 398.9, 400.8 and 401.2 eV correspond to the C≡N-C, N-(C)<sub>3</sub> and C-NH<sub>x</sub>, respectively. The N 1 s binding energy of N = C-N heptazine rings (399.2 eV) of Pt-Tb<sub>4</sub>O<sub>7</sub>/CN-4.5 is higher than that (398.9 eV) of Tb<sub>4</sub>O<sub>7</sub>/CN, suggesting that the presence of an interaction between N and metallic Pt in Pt-Tb<sub>4</sub>O<sub>7</sub>/CN-4.5 photocatalyst. This result supports that Pt is loaded on the CN section of Pt-Tb<sub>4</sub>O<sub>7</sub>/CN-4.5, agreeing well with the HRTEM analysis result and the HR-XPS analysis result of Pt 4 f. The N1s binding

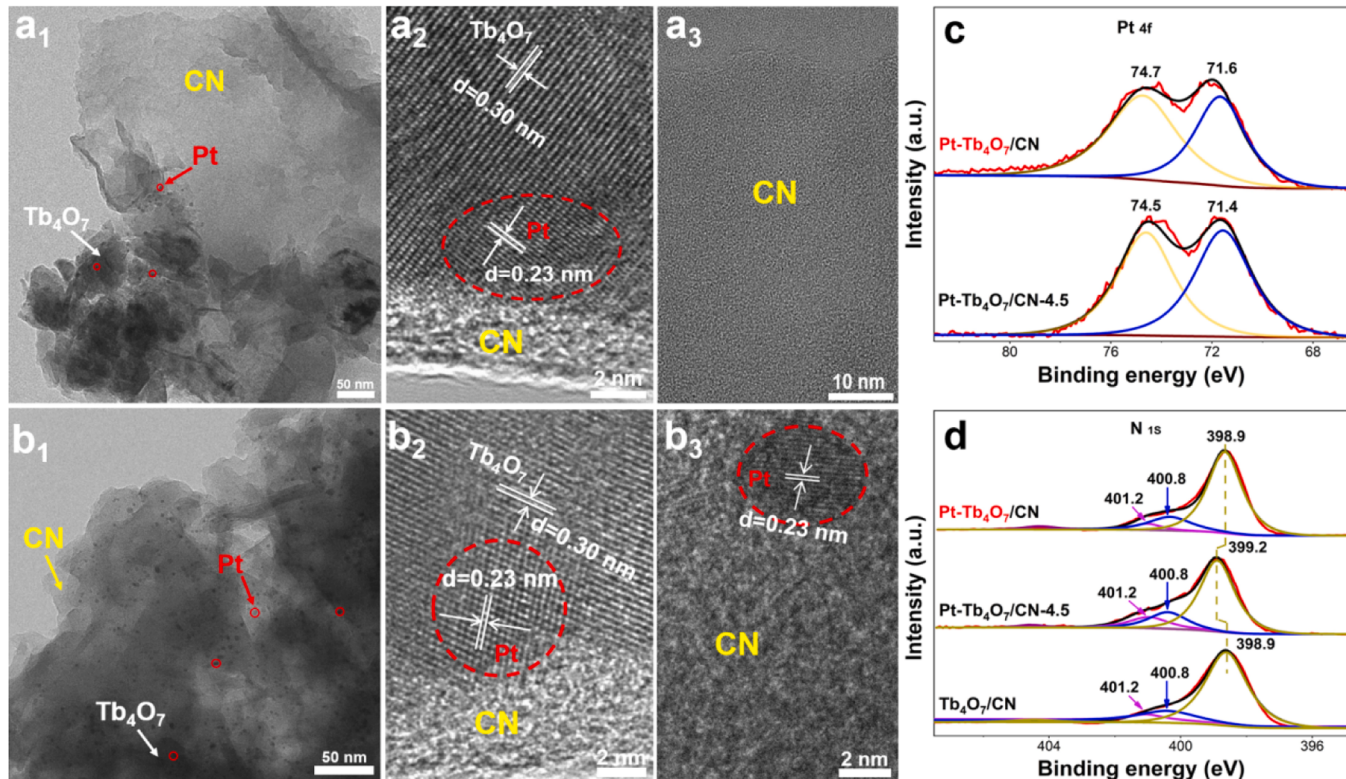


**Fig. 2.** (a<sub>1</sub>) TEM image and (a<sub>2</sub>-a<sub>3</sub>) HRTEM images of Pt-Tb<sub>4</sub>O<sub>7</sub>/CN, (b<sub>1</sub>) TEM image and (b<sub>2</sub>-b<sub>3</sub>) HRTEM images of Pt-Tb<sub>4</sub>O<sub>7</sub>/CN-4.5, (c) HR-XPS spectra of Pt 4 f, (d) HR-XPS spectra of N 1 s of Pt-Tb<sub>4</sub>O<sub>7</sub>/CN, Pt-Tb<sub>4</sub>O<sub>7</sub>/CN-4.5 and Tb<sub>4</sub>O<sub>7</sub>/CN.

energy ( $C=N-C$ ) of Pt-Tb<sub>4</sub>O<sub>7</sub>/CN is the same as that of Tb<sub>4</sub>O<sub>7</sub>/CN heterojunction, further verifying that Pt is not loaded on CN but on the Tb<sub>4</sub>O<sub>7</sub> section of Pt-Tb<sub>4</sub>O<sub>7</sub>/CN. Based on the above characterizations, one can conclude that the selective loading of Pt on Tb<sub>4</sub>O<sub>7</sub> has been achieved for Pt-Tb<sub>4</sub>O<sub>7</sub>/CN, while the loading of Pt for Pt-Tb<sub>4</sub>O<sub>7</sub>/CN-4.5 is non-selective.

### 3.1.2. Optical and electrical performances

**Fig. 3a** gives the UV-vis diffuse reflection spectra of Tb<sub>4</sub>O<sub>7</sub>/CN, Pt-Tb<sub>4</sub>O<sub>7</sub>/CN-4.5 and Pt-Tb<sub>4</sub>O<sub>7</sub>/CN. Compared to the Tb<sub>4</sub>O<sub>7</sub>/CN heterojunction, the absorption edge of Pt-Tb<sub>4</sub>O<sub>7</sub>/CN-4.5 and Pt-Tb<sub>4</sub>O<sub>7</sub>/CN display no obvious red/blue-shift. The Pt loading does not significantly affect the band gaps (Fig. S8). Nevertheless, the optical absorption intensities for both Pt-Tb<sub>4</sub>O<sub>7</sub>/CN-4.5 and Pt-Tb<sub>4</sub>O<sub>7</sub>/CN increase in the long-wavelength region; compared to that of Tb<sub>4</sub>O<sub>7</sub>/CN, which is owing to localized surface plasma resonance of the metallic Pt loaded on Tb<sub>4</sub>O<sub>7</sub>/CN [48]. **Fig. 3b** shows the photoluminescence (PL) spectra of Tb<sub>4</sub>O<sub>7</sub>/CN, Pt-Tb<sub>4</sub>O<sub>7</sub>/CN-4.5 and Pt-Tb<sub>4</sub>O<sub>7</sub>/CN photocatalysts. Pt-Tb<sub>4</sub>O<sub>7</sub>/CN exhibits a greatly decreased PL intensity compared to Tb<sub>4</sub>O<sub>7</sub>/CN, indicating that the completely selective Pt loading on Tb<sub>4</sub>O<sub>7</sub> greatly declines the electron-hole pairs recombination [49]. However, Pt-Tb<sub>4</sub>O<sub>7</sub>/CN-4.5 displays a slightly increased PL intensity in comparison with Tb<sub>4</sub>O<sub>7</sub>/CN, suggesting a higher charge carrier recombination due to partially non-selective Pt loading on CN (see Section 3.3). The time-resolved PL decay spectra (Fig. 3c and Table S1) show that the PL lifetimes of Tb<sub>4</sub>O<sub>7</sub>/CN, Pt-Tb<sub>4</sub>O<sub>7</sub>/CN-4.5 and Pt-Tb<sub>4</sub>O<sub>7</sub>/CN are 10.34, 9.98 and 12.89 ns, respectively. The longest PL lifetime (12.89 ns) for Pt-Tb<sub>4</sub>O<sub>7</sub>/CN indicates the lowest electron-hole pairs recombination rate, in line with the result from Fig. 3b. The highest photocurrent (Fig. 3d) of the as-prepared Pt-Tb<sub>4</sub>O<sub>7</sub>/CN further reveals that the precise loading of metallic Pt on Tb<sub>4</sub>O<sub>7</sub> greatly promotes the charge separation. **Fig. 3e** shows the electrochemical impedance spectra (EIS) of Tb<sub>4</sub>O<sub>7</sub>/CN, Pt-Tb<sub>4</sub>O<sub>7</sub>/CN-4.5 and Pt-Tb<sub>4</sub>O<sub>7</sub>/CN photocatalysts. The smallest semicircle at high frequency represents the lowest interfacial charge

transport resistance ( $R_{ct}$ ) [50]. Among them, the Pt-Tb<sub>4</sub>O<sub>7</sub>/CN possesses the smallest semicircle ( $R_{ct} = 1386 \Omega \text{ cm}^2$ ) while the Tb<sub>4</sub>O<sub>7</sub>/CN has the largest semicircle ( $R_{ct} = 1757 \Omega \text{ cm}^2$ ), verifying that the loading Pt on Tb<sub>4</sub>O<sub>7</sub>/CN can efficiently reduce interfacial charge transport resistance. **Fig. 3f** shows the linear sweep voltammetry (LSV) curves of Tb<sub>4</sub>O<sub>7</sub>/CN, Pt-Tb<sub>4</sub>O<sub>7</sub>/CN-4.5 and Pt-Tb<sub>4</sub>O<sub>7</sub>/CN photocatalysts. The overpotentials of both Pt-Tb<sub>4</sub>O<sub>7</sub>/CN-4.5 and Pt-Tb<sub>4</sub>O<sub>7</sub>/CN photocatalysts are decreased in comparison with the pristine Tb<sub>4</sub>O<sub>7</sub>/CN. The decrease of the overpotentials can be attributed to the extremely high intrinsic HER activity of Pt [51]. Pt-Tb<sub>4</sub>O<sub>7</sub>/CN-4.5 exhibits a lower HER activity than Pt-Tb<sub>4</sub>O<sub>7</sub>/CN because of the difference in the charge transport resistance.

### 3.1.3. POWS performance

POWS performance of Tb<sub>4</sub>O<sub>7</sub>/CN, Pt-Tb<sub>4</sub>O<sub>7</sub>/CN-4.5 and Pt-Tb<sub>4</sub>O<sub>7</sub>/CN photocatalysts were evaluated by H<sub>2</sub>-evolving rate under visible light ( $\lambda > 420 \text{ nm}$ ) irradiation. As is shown in Fig. 4a, Pt-Tb<sub>4</sub>O<sub>7</sub>/CN photocatalyst exhibits a vigorously enhanced POWS activity with a H<sub>2</sub> evolution rate of  $132 \mu\text{mol h}^{-1} \text{ g}^{-1}$ , about 2.8 times as high as that of the Tb<sub>4</sub>O<sub>7</sub>/CN heterojunction. Simultaneously, the H<sub>2</sub>O<sub>2</sub> is produced with a rate of  $130 \mu\text{mol h}^{-1} \text{ g}^{-1}$ , demonstrating that the POWS is a two-electron reaction process ( $2 \text{ H}_2\text{O} \rightarrow \text{H}_2 + \text{H}_2\text{O}_2$ ) [52]. No O<sub>2</sub> can be detected in the reaction system. This enhanced POWS activity of Pt-Tb<sub>4</sub>O<sub>7</sub>/CN can be ascribed to the improved charge separation and high HER activity from the oriented Pt loading. However, Pt-Tb<sub>4</sub>O<sub>7</sub>/CN-4.5 displays a slightly declined POWS activity ( $42.9 \mu\text{mol h}^{-1} \text{ g}^{-1}$  for H<sub>2</sub> evolution and  $40.8 \mu\text{mol h}^{-1} \text{ g}^{-1}$  for H<sub>2</sub>O<sub>2</sub> production) compared to the pristine Tb<sub>4</sub>O<sub>7</sub>/CN heterojunction ( $48.9 \mu\text{mol h}^{-1} \text{ g}^{-1}$  for H<sub>2</sub> evolution and  $47.1 \mu\text{mol h}^{-1} \text{ g}^{-1}$  for H<sub>2</sub>O<sub>2</sub> production). The slight decreased POWS performance is mainly contributed to the increased charge recombination (Fig. 3b-c) and higher charge transport resistance (Fig. 3e).

**Fig. 4b** displays UV-Vis diffuse reflectance spectrum and AQY of Pt-Tb<sub>4</sub>O<sub>7</sub>/CN at different monochromatic wavelengths. The AQY values at 420, 450 and 470 nm for photocatalytic H<sub>2</sub> production are 5.9%, 1.6%

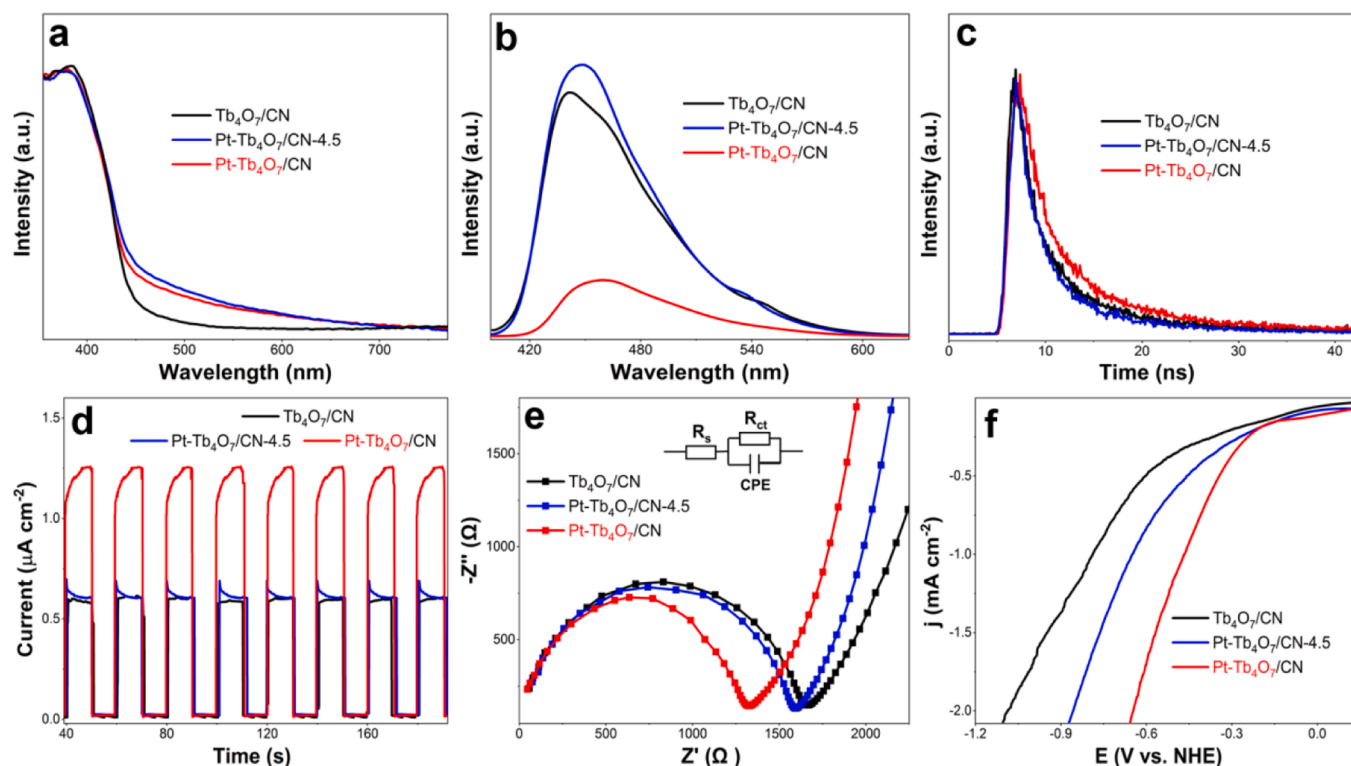


**Fig. 3.** (a) UV-vis diffuse reflection spectra, (b) PL emission spectra, (c) Time-resolve PL decay spectra, (d) Photocurrent response curves, (e) EIS, (f) LSV plots of Tb<sub>4</sub>O<sub>7</sub>/CN, Pt-Tb<sub>4</sub>O<sub>7</sub>/CN-4.5 and Pt-Tb<sub>4</sub>O<sub>7</sub>/CN photocatalysts.

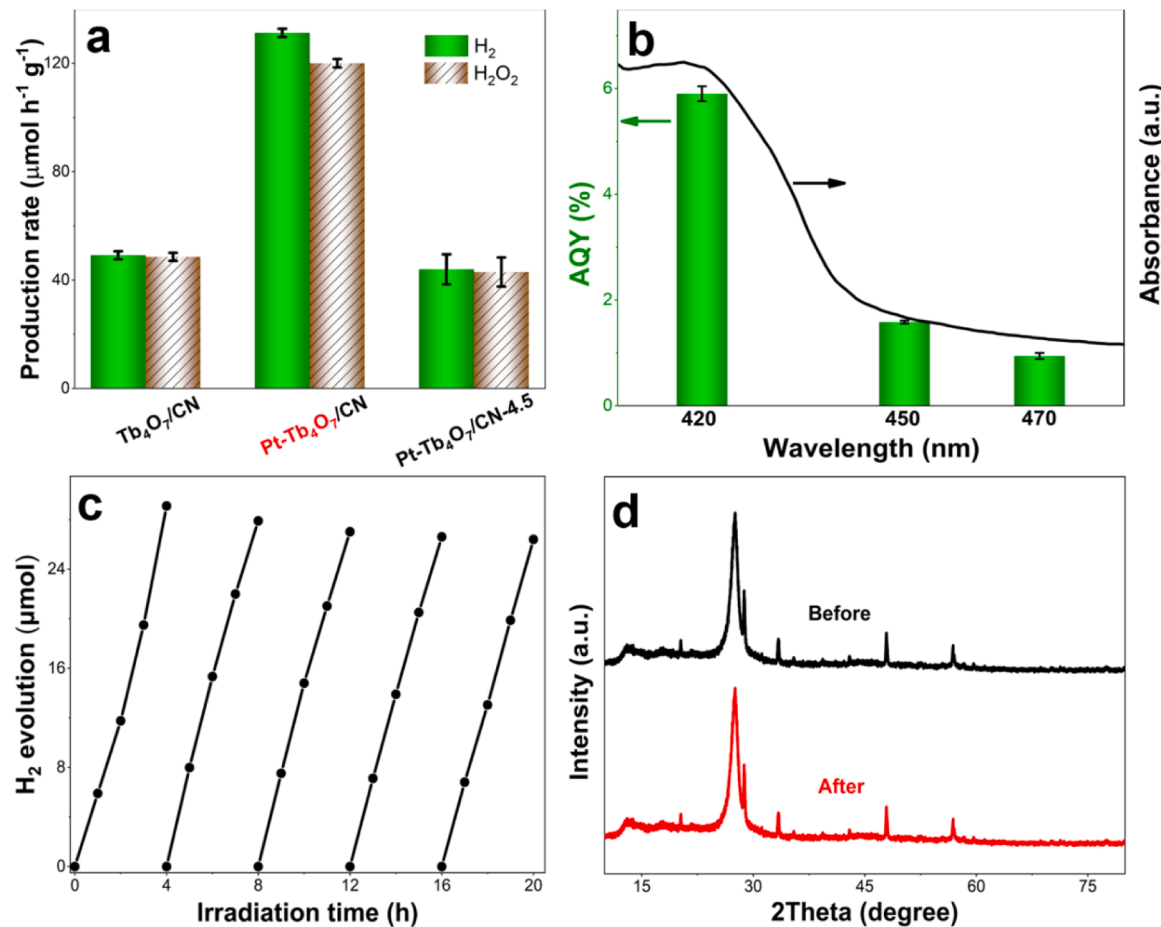


**Fig. 4.** (a) POWS activity of  $\text{Tb}_4\text{O}_7/\text{CN}$ ,  $\text{Pt-Tb}_4\text{O}_7/\text{CN-4.5}$  and  $\text{Pt-Tb}_4\text{O}_7/\text{CN}$  photocatalysts for  $\text{H}_2$  and  $\text{H}_2\text{O}_2$  production. (b) UV-Vis diffuse reflectance spectrum and AQY of  $\text{Pt-Tb}_4\text{O}_7/\text{CN}$  at different monochromatic wavelengths for POWS. (c) Stability test of  $\text{Pt-Tb}_4\text{O}_7/\text{CN}$  for POWS. (d) XRD patterns of  $\text{Pt-Tb}_4\text{O}_7/\text{CN}$  before and after 20 h POWS.

and 0.96%, respectively. The rapid decline of AQY with the increasing radiation wavelength suggests that the  $\text{H}_2$  generation is driven by light irradiation. Notably, the as-prepared  $\text{Pt-Tb}_4\text{O}_7/\text{CN}$  photocatalyst exhibits an excellent POWS performance in comparison with the recently reported CN-based heterojunction photocatalysts (Table S2). As shown in Fig. 4c, the  $\text{Pt-Tb}_4\text{O}_7/\text{CN}$  is stable in 5 uninterrupted cycles for 20 h irradiation. After 20 h reaction, the XRD pattern of the utilized  $\text{Pt-Tb}_4\text{O}_7/\text{CN}$  photocatalyst is in line with that of the initial sample (Fig. 4d), and the unique sandwich morphology and Pt chemical state of  $\text{Pt-Tb}_4\text{O}_7/\text{CN}$  photocatalyst remain unchanged (Fig. S9 and Fig. S10), further verifying the superior stability of  $\text{Pt-Tb}_4\text{O}_7/\text{CN}$  photocatalyst.

The effects of Pt loading content at pH 7.8 and photo-deposition pH on the POWS activity of  $\text{Pt-Tb}_4\text{O}_7/\text{CN-x}$  photocatalysts were investigated. The optimal Pt loading content and photo-deposition pH value are determined to be 0.30 wt% (Fig. S11a) and 7.8 (Fig. S11b), respectively. As shown in Fig. S11b, when pH value is above 7.8, the reduced POWS activity is attributed to the decreased Pt loading content (Fig. S7) at pH 9.0 and 10, respectively. At pH 6.8, although the Pt loading content (0.31 wt%) is close to the optimal 0.30 wt% for  $\text{Pt-Tb}_4\text{O}_7/\text{CN}$ , the POWS activity of  $\text{Pt-Tb}_4\text{O}_7/\text{CN-6.8}$  is significantly lower than that of  $\text{Pt-Tb}_4\text{O}_7/\text{CN}$ . The HR-XPS spectrum of N 1 s of  $\text{Pt-Tb}_4\text{O}_7/\text{CN-6.8}$  is similar to the spectra of  $\text{Pt-Tb}_4\text{O}_7/\text{CN}$  and  $\text{Tb}_4\text{O}_7/\text{CN}$  (Fig. S12), verifying that Pt is also selectively loaded on  $\text{Tb}_4\text{O}_7$  section of  $\text{Tb}_4\text{O}_7/\text{CN}$  rather than on CN section. The TEM images show that the mean size of Pt nanoparticles for  $\text{Pt-Tb}_4\text{O}_7/\text{CN-6.8}$  and  $\text{Pt-Tb}_4\text{O}_7/\text{CN}$  are 6.7 and 4.4 nm (Fig. S13), respectively. These results manifest that tuning the deposition pH can effectively control the size of the deposition Pt and thus can influence the POWS activity.

### 3.2. Orient loading of Pt on CN of $\text{Tb}_4\text{O}_7/\text{CN}$ and its effect on POWS

#### 3.2.1. Design, preparation and characterization

To further investigate the effect of the Pt loading on CN and its impact on POWS performance, a contrast sample ( $\text{Tb}_4\text{O}_7/\text{CN-Pt}$ ) was designed and prepared using  $[\text{Pt}(\text{NH}_3)_4]^{2+}$  to replace  $[\text{PtCl}_6]^{2-}$  under the same conditions as those for  $\text{Pt-Tb}_4\text{O}_7/\text{CN}$ . Fig. 5a visually illustrates the preparation process of  $\text{Tb}_4\text{O}_7/\text{CN-Pt}$ . It is shown that  $[\text{Pt}(\text{NH}_3)_4]^{2+}$  is selectively adsorbed on the CN rather than on  $\text{Tb}_4\text{O}_7$  due to the electrostatic interaction between  $[\text{Pt}(\text{NH}_3)_4]^{2+}$  and the CN of CN/ $\text{Tb}_4\text{O}_7$  at pH 7.8 (Fig. S3). After irradiation,  $[\text{Pt}(\text{NH}_3)_4]^{2+}$  is photo-deposited on CN in metallic Pt, which realizes the oriented loading Pt on the CN section of  $\text{Tb}_4\text{O}_7/\text{CN}$ . ICP-AES analysis indicates that the Pt loading amount of  $\text{Tb}_4\text{O}_7/\text{CN-Pt}$  is equivalent to that of  $\text{Pt-Tb}_4\text{O}_7/\text{CN}$  prepared by using  $[\text{PtCl}_6]^{2-}$ .

The TEM image of  $\text{Tb}_4\text{O}_7/\text{CN-Pt}$  (Fig. 5b<sub>1</sub>) reveals that Pt particles are loaded on  $\text{Tb}_4\text{O}_7/\text{CN}$ . The HRTEM images of  $\text{Tb}_4\text{O}_7/\text{CN-Pt}$  show that no Pt particle can be found in the  $\text{Tb}_4\text{O}_7$  section (Fig. 5b<sub>2</sub>), while metallic Pt can be discovered on CN section (Fig. 5b<sub>3</sub>) because the lattice fringe space of 0.23 nm relates to the (111) crystallographic plane of metallic Pt. Fig. 5c shows that the obvious blue-shift of the binding energy peak of N = C-N heptazine rings observed in the HR-XPS spectrum of N 1 s of  $\text{Tb}_4\text{O}_7/\text{CN-Pt}$  compared to that of  $\text{Tb}_4\text{O}_7/\text{CN}$ , shifting from 398.9 to 399.5 eV, further indicating the Pt is loaded selectively on CN section of  $\text{Tb}_4\text{O}_7/\text{CN-Pt}$ . Summarily, with the help of surface charge engineering and photoreduction strategy, selective loading of metallic Pt on CN of  $\text{Tb}_4\text{O}_7/\text{CN}$  for  $\text{Tb}_4\text{O}_7/\text{CN-Pt}$  photocatalyst is achieved.

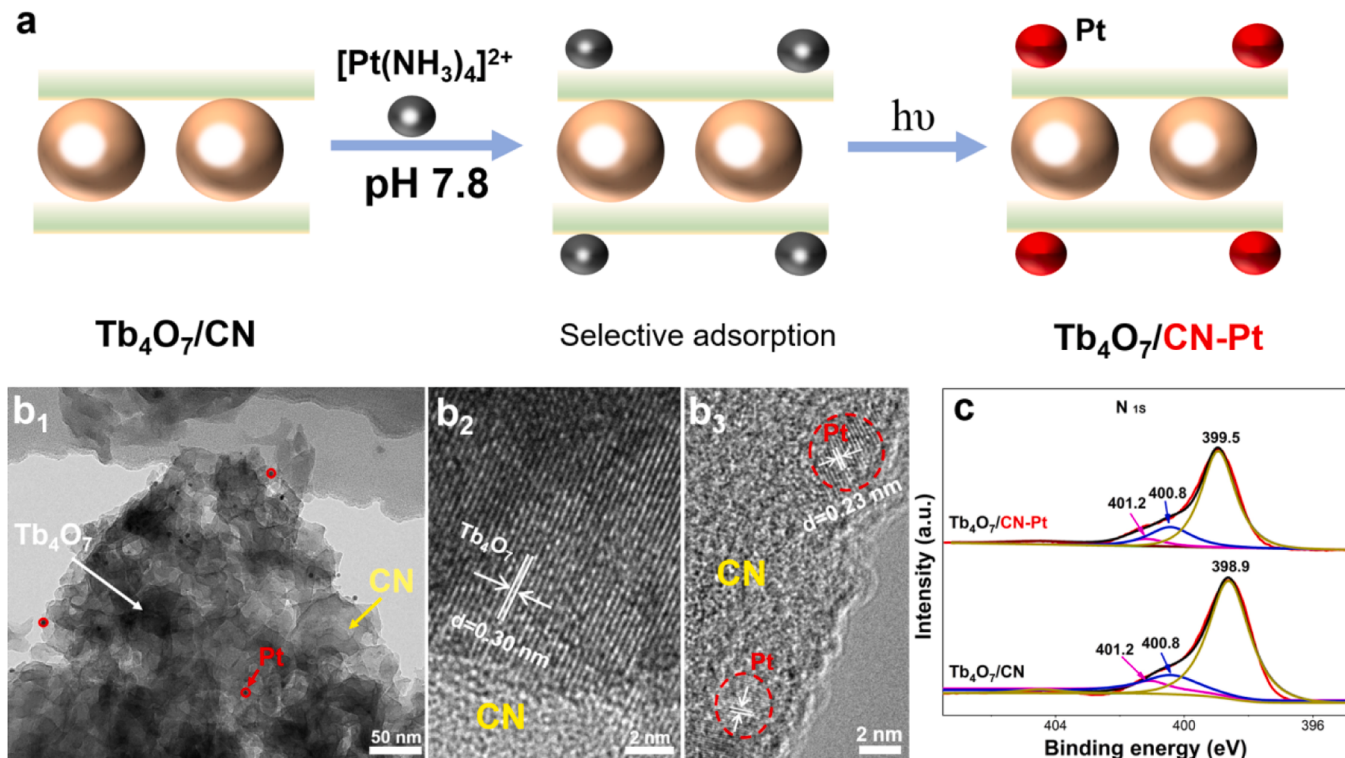


**Fig. 5.** (a) Schematic diagram of the preparation process of Tb<sub>4</sub>O<sub>7</sub>/CN-Pt. (b<sub>1</sub>) TEM image and (b<sub>2</sub>-b<sub>3</sub>) HRTEM images of Tb<sub>4</sub>O<sub>7</sub>/CN-Pt, (c) HR-XPS spectra of N 1 s of Tb<sub>4</sub>O<sub>7</sub>/CN and Tb<sub>4</sub>O<sub>7</sub>/CN-Pt photocatalysts.

### 3.2.2. Physicochemical and POWS performances

Fig. 6a shows that besides the optical absorption intensity displays a remarkable enhancement in the long wavelength range, the absorption

edge of Tb<sub>4</sub>O<sub>7</sub>/CN-Pt appears an obvious red-shift, compared to the Tb<sub>4</sub>O<sub>7</sub>/CN heterojunction. The red-shift extends light absorption range of Tb<sub>4</sub>O<sub>7</sub>/CN-Pt, agreeing with the darker color digital photograph.

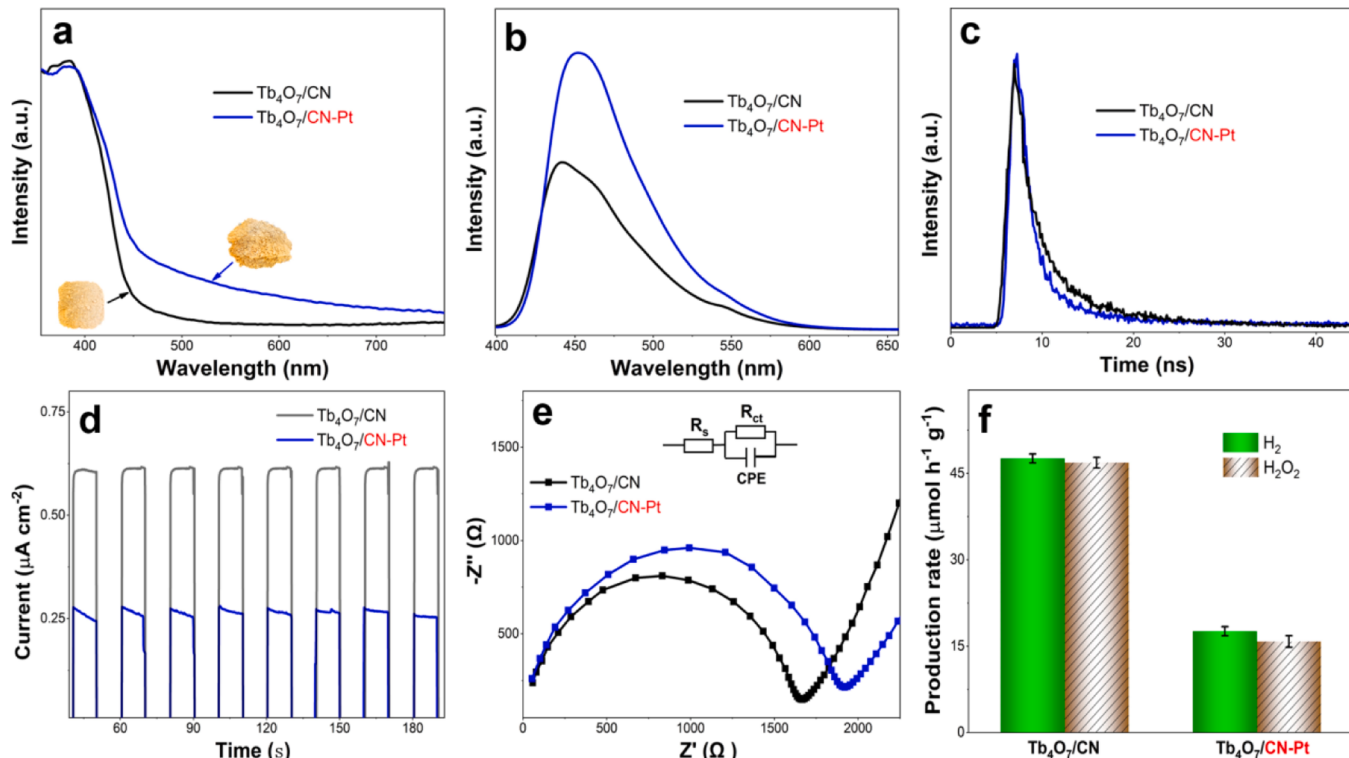


**Fig. 6.** (a) UV-vis diffuse reflection spectra, (b) PL emission spectra and (c) Time-resolved PL decay spectra, (d) Photocurrent response curves, (e) EIS, (f) POWS performance of Tb<sub>4</sub>O<sub>7</sub>/CN and Tb<sub>4</sub>O<sub>7</sub>/CN-Pt.

According to the Kubelka-Munk function, the band gap energy of  $\text{Tb}_4\text{O}_7/\text{CN}$ -Pt is determined to be 2.55 eV which is narrower than that of  $\text{Tb}_4\text{O}_7/\text{CN}$  heterojunction (2.67 eV) (Fig. S14). The red-shift of the optical absorption edge and the increased optical absorption intensity are attributed to the strong interaction between Pt and CN and the localized surface plasma resonance of the Pt loading on  $\text{Tb}_4\text{O}_7/\text{CN}$ , respectively. The increased PL intensity for  $\text{Tb}_4\text{O}_7/\text{CN}$ -Pt (Fig. 6b) and the shorted PL lifetime (8.89 ns) (Fig. 6c and Table S1) suggest a faster recombination of photoexcited electron-hole pairs in comparison with  $\text{Tb}_4\text{O}_7/\text{CN}$  owing to completely selective Pt loading on CN (see Section 3.3). The lower transient photocurrent density of the  $\text{Tb}_4\text{O}_7/\text{CN}$ -Pt photocatalyst than that of  $\text{Tb}_4\text{O}_7/\text{CN}$  (Fig. 6d) indicates a low-effective charge separation, that is, the fast photogenerated charge carrier recombination. Fig. 6e appears a bigger semicircle for  $\text{Tb}_4\text{O}_7/\text{CN}$ -Pt in EIS spectra at high frequency than that for  $\text{Tb}_4\text{O}_7/\text{CN}$ , signifying a larger interfacial charge transport resistance ( $R_{ct} = 1974 \Omega \text{ cm}^{-1}$ ). Fig. S15 shows a smaller overpotential of  $\text{Tb}_4\text{O}_7/\text{CN}$ -Pt than that of  $\text{Tb}_4\text{O}_7/\text{CN}$ , owing to the extremely high intrinsic HER activity of Pt. As is shown in Fig. 6f, the  $\text{Tb}_4\text{O}_7/\text{CN}$ -Pt photocatalyst possesses a remarkably declined POWS performance. The  $\text{H}_2$  evolution and  $\text{H}_2\text{O}_2$  production rate are 18.2 and 16.5  $\mu\text{mol h}^{-1} \text{ g}^{-1}$ , respectively; about 2.6 times as low as that of pristine  $\text{Tb}_4\text{O}_7/\text{CN}$ . The rational explanation is that loading Pt on CN of  $\text{Tb}_4\text{O}_7/\text{CN}$  leads to accelerating the photoinduced electron-hole pairs recombination. This result clearly demonstrates that the loading site of Pt plays a key role in POWS performance.

### 3.3. Photocatalytic mechanism: synergistic and anti-synergistic effects of Pt loading sites

The conductor band (CB) energies of  $\text{Tb}_4\text{O}_7$  and CN are  $-3.81$  and  $-3.46$  eV vs. vacuum level (assumed to be 0 eV) [32], and their valence

band (VB) energies are  $-6.88$  and  $-6.18$  eV, respectively. Because both  $\text{Tb}_4\text{O}_7$  and CN are n type semiconductors [32,53], their Fermi levels (FLs) locate below and near their CB energies, respectively [54, 55]. The N1s and Tb 5p 3/2 XPS spectra verify the presence of the electron transfer from CN to  $\text{Tb}_4\text{O}_7$  in  $\text{Tb}_4\text{O}_7/\text{CN}$  heterojunction [32], suggesting that the FL of  $\text{Tb}_4\text{O}_7$  is lower than that of CN. Since the FL value of Pt is  $-5.93$  eV [56,57], the FL values in both Pt- $\text{Tb}_4\text{O}_7/\text{CN}$  and  $\text{Tb}_4\text{O}_7/\text{CN}$ -Pt heterojunctions follow the order: Pt <  $\text{Tb}_4\text{O}_7$  < CN. Thus, electrons are prone to enrich on Pt in the two heterojunctions. When Pt,  $\text{Tb}_4\text{O}_7$  and CN tightly contact, their FLs are aligned. Those energy levels and possible charge transport paths are illustrated in Fig. 7. The band gap energies of  $\text{Tb}_4\text{O}_7$  and CN are 3.07 and 2.72 eV, respectively. Therefore, when the Pt- $\text{Tb}_4\text{O}_7/\text{CN}$  and  $\text{Tb}_4\text{O}_7/\text{CN}$ -Pt photocatalysts are irradiated by visible light, only CN can be excited to produce electrons and holes. Fig. 7a exhibits the charges separation/transport behavior of Pt- $\text{Tb}_4\text{O}_7/\text{CN}$  photocatalyst, where the photogenerated electrons in the CB of CN inject to the CB of  $\text{Tb}_4\text{O}_7$  and subsequently transfer to metallic Pt whereas the photogenerated holes are blocked by  $\text{Tb}_4\text{O}_7$  owing to the higher VB of CN than that of  $\text{Tb}_4\text{O}_7$ , effectively realizing the photogenerated electron-hole pairs separation in space (Figs. 3b-3d). As a result, the POWS performance significantly enhances. In this case, the loading site of Pt is compatible with the photogenerated charge transfer of CN/ $\text{Tb}_4\text{O}_7$ , which is called the synergistic effect of Pt loading sites. Contrarily, when the metallic Pt is loaded on CN of  $\text{Tb}_4\text{O}_7/\text{CN}$ -Pt photocatalyst (Fig. 7b), photoexcited electrons are easily collected on metallic Pt due to its low FL [58], and simultaneously the photoexcited holes in VB of CN can also transfer to Pt due to the lower VB than the EL of Pt, leading to the local recombination of photogenerated electron-hole pairs, although  $\text{Tb}_4\text{O}_7/\text{CN}$  promotes the separation and transmission of photogenerated charge carriers. In this case, the loading site of Pt is incompatible with the photogenerated charge transfer of

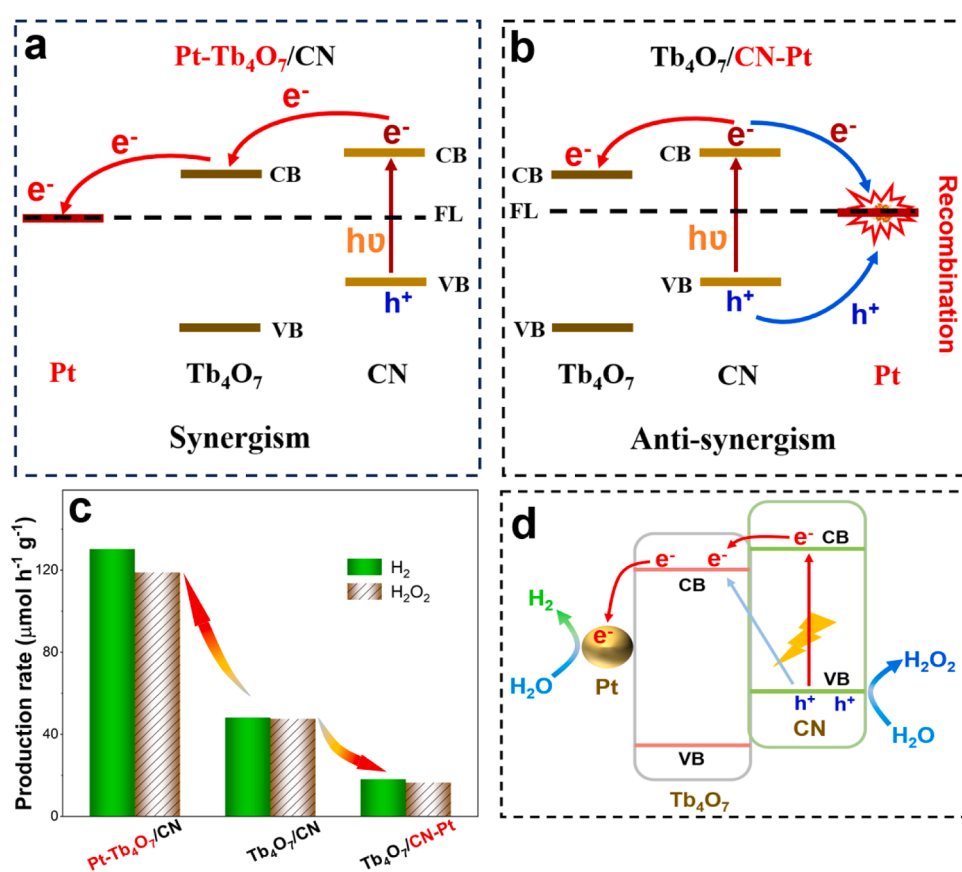


Fig. 7. Schematic diagrams of Pt loading effects on photogenerated charge separation/transfer of (a) Pt- $\text{Tb}_4\text{O}_7/\text{CN}$  and (b)  $\text{Tb}_4\text{O}_7/\text{CN}$ -Pt. (c) Comparison of POWS activities of Pt- $\text{Tb}_4\text{O}_7/\text{CN}$ ,  $\text{Tb}_4\text{O}_7/\text{CN}$  and  $\text{Tb}_4\text{O}_7/\text{CN}$ -Pt photocatalysts. (d) Schematic diagram of the photocatalytic mechanism for Pt- $\text{Tb}_4\text{O}_7/\text{CN}$ .

CN/Tb<sub>4</sub>O<sub>7</sub>, which is called the anti-synergistic effect of Pt loading sites. Notably, the synergistic effect of Pt loading enhances the POWS performance of Pt-Tb<sub>4</sub>O<sub>7</sub>/CN with a H<sub>2</sub> evolution rate of 132 μmol h<sup>-1</sup> g<sup>-1</sup> (Fig. 7c), whereas the anti-synergistic effect of Pt loading declines the POWS performance of Tb<sub>4</sub>O<sub>7</sub>/CN-Pt with a H<sub>2</sub> evolution rate of 18.2 μmol h<sup>-1</sup> g<sup>-1</sup> (Fig. 7c). Overall, Pt-Tb<sub>4</sub>O<sub>7</sub>/CN shows around 7 times higher POWS activity than Tb<sub>4</sub>O<sub>7</sub>/CN-Pt, indicating the importance of selective loading Pt on Tb<sub>4</sub>O<sub>7</sub>/CN.

There are two pathways for photogenerated charge transfer in Tb<sub>4</sub>O<sub>7</sub>/CN: the direct model and the indirect model [32]. Indirect photoinduced charge transfer includes two steps: the excited electrons firstly jump from the VB of CN to the CB of CN, and then inject to the CB of Tb<sub>4</sub>O<sub>7</sub>, which has been confirmed by the differential spectrum of pristine CN, Tb<sub>4</sub>O<sub>7</sub> and Tb<sub>4</sub>O<sub>7</sub>/CN [32,53]. The direct charge transfer is achieved by direct photoinduced electrons transfer from the VB of CN to the CB of Tb<sub>4</sub>O<sub>7</sub>. Because the POWS activity of Tb<sub>4</sub>O<sub>7</sub>/CN-Pt is greatly declined in comparison with Tb<sub>4</sub>O<sub>7</sub>/CN, one can conclude that the direct charge transfer from the VB of CN to CB of Tb<sub>4</sub>O<sub>7</sub> is minor, testifying that the indirect charge transfer model is major.

As is shown in Fig. 7d, the mechanism of POWS performance of Pt-Tb<sub>4</sub>O<sub>7</sub>/CN is depicted. Under visible light irradiation, electrons migrate from the VB of CN to the CB of CN/ Tb<sub>4</sub>O<sub>7</sub> via the two models and subsequently are collected on metallic Pt to reduce the adsorbed H<sub>2</sub>O to evolve H<sub>2</sub>. Simultaneously, the photoinduced holes in-situ oxidize the adsorbed H<sub>2</sub>O to produce H<sub>2</sub>O<sub>2</sub>. Pt-Tb<sub>4</sub>O<sub>7</sub>/CN possesses a high POWS activity, which can be mainly contributed to the synergistic effect of loading Pt that promotes the charge separation. Besides, the high intrinsic HER activity and low resistance of heterojunction also improve the POWS performance of Pt-Tb<sub>4</sub>O<sub>7</sub>/CN.

#### 4. Conclusion

In conclusion, the oriented loading of Pt on Tb<sub>4</sub>O<sub>7</sub>/CN heterojunction has been achieved by surface charge engineering and photo-reduction technique using two different Pt precursors: [PtCl<sub>6</sub>]<sup>2-</sup> and [Pt(NH<sub>3</sub>)<sub>4</sub>]<sup>2+</sup>. As the [PtCl<sub>6</sub>]<sup>2-</sup> is adopted, Pt is selectively loaded on Tb<sub>4</sub>O<sub>7</sub> section of Tb<sub>4</sub>O<sub>7</sub>/CN (Pt-Tb<sub>4</sub>O<sub>7</sub>/CN) at pH 7.8. While when [Pt (NH<sub>3</sub>)<sub>4</sub>]<sup>2+</sup> is employed, the metallic Pt is selectively loaded on the CN section of Tb<sub>4</sub>O<sub>7</sub>/CN (Tb<sub>4</sub>O<sub>7</sub>/CN-Pt) at pH 7.8. For Pt-Tb<sub>4</sub>O<sub>7</sub>/CN, the Pt loading site is compatible with the charge separation of Tb<sub>4</sub>O<sub>7</sub>/CN heterojunction, promoting the photogenerated charge separation. As a result, the POWS activity enhances greatly. The H<sub>2</sub> production rate is up to 132 μmol h<sup>-1</sup> g<sup>-1</sup>, accompanying with stoichiometric H<sub>2</sub>O<sub>2</sub> production, about 2.8 times as high as the Tb<sub>4</sub>O<sub>7</sub>/CN. The AQY for H<sub>2</sub> evolution at 420 nm reaches to 5.9%. In contrast, for Tb<sub>4</sub>O<sub>7</sub>/CN-Pt, the Pt loading site is incompatible with the charge separation of Tb<sub>4</sub>O<sub>7</sub>/CN heterojunction, leading to a greatly increase in the photogenerated electron-hole pairs recombination. Therefore, the POWS activity deactivates greatly, about 2.6 times as low as that of Tb<sub>4</sub>O<sub>7</sub>/CN. Pt-Tb<sub>4</sub>O<sub>7</sub>/CN shows around 7 times higher POWS activity than Tb<sub>4</sub>O<sub>7</sub>/CN-Pt, indicating the importance of selective loading Pt on Tb<sub>4</sub>O<sub>7</sub>/CN. The findings provide insights on design, preparation and mechanism of coupling HER co-catalysts with heterojunction photocatalysts for POWS.

#### CRediT authorship contribution statement

**Dedong Zeng:** Investigation, Methodology, Visualization, Writing – original draft. **Yuexiang Li:** Conceptualization, Methodology, Writing – review & editing, Resources, Funding acquisition, Supervision.

#### Declaration of Competing Interest

The authors declare that they have no known competing financial interests or personal relationships that could have appeared to influence the work reported in this paper.

#### Data Availability

Data will be made available on request.

#### Acknowledgments

This work was supported by the National Natural Science Foundation of China (21962010, 22362021) and the National Key Research and Development Program of China (2018YFB1502004). Zeng thanks Dr. Lingling Liu and Prof. Yu Xie of the College of Environment and Chemical Engineering, Nanchang Hangkong University, for XPS and SEM characterization.

#### Appendix A. Supporting information

Supplementary data associated with this article can be found in the online version at doi:10.1016/j.apcatb.2023.123393.

#### References

- [1] X.J. Chen, J. Wang, Y.Q. Chai, Z.J. Zhang, Y.F. Zhu, Efficient photocatalytic overall water splitting induced by the giant internal electric field of a g-C<sub>3</sub>N<sub>4</sub>/rGO/PPDIP Z-scheme heterojunction, *Adv. Mater.* 33 (2021) 2007479.
- [2] F. He, Z.X. Wang, Y.X. Li, S.Q. Peng, B. Liu, The nonmetal modulation of composition and morphology of g-C<sub>3</sub>N<sub>4</sub>-based photocatalysts, *Appl. Catal. B-Environ.* 269 (2020), 118828.
- [3] Y. Wang, A. Vogel, M. Sachs, R.S. Sprick, L. Wilbraham, S.J.A. Moniz, R. Godin, M. A. Zwijnenburg, J.R. Durrant, A.I. Cooper, J.W. Tang, Current understanding and challenges of solar-driven hydrogen generation using polymeric photocatalysts, *Nat. Energy* 4 (2019) 746–760.
- [4] D.D. Zeng, L.M. Yang, P.P. Zhou, D.S. Hu, Y. Xie, S.Q. Li, L.S. Jiang, Y. Ling, J. S. Zhao, Au Cu alloys deposited on titanium dioxide nanosheets for efficient photocatalytic hydrogen evolution, *Int. J. Hydrol. Energy* 43 (2018) 15155–15163.
- [5] V.L. Dagle, G. Collinge, M. Rahman, A. Winkelmann, W.D. Hu, J.Z. Hu, L. Kovarik, M. Engelhard, J. Jocic, Y. Wang, M.S. Lee, V.A. Glezakou, D. Ray, R. Rousseau, R. Dagle, Single-step conversion of ethanol into n-butene-rich olefins over metal catalysts supported on ZrO<sub>2</sub>-SiO<sub>2</sub> mixed oxides, *Appl. Catal. B-Environ.* 331 (2023), 122707.
- [6] D.M. Zhao, Y.Q. Wang, C.L. Dong, Y.C. Huang, J. Chen, F. Xue, S.H. Shen, L.J. Guo, Boron-doped nitrogen-deficient carbon nitride-based Z-scheme heterostructures for photocatalytic overall water splitting, *Nat. Energy* 6 (2021) 388–397.
- [7] Z.Y. Wu, Q. Hong, X.T. Wang, H. Shi, T.Y. Zhang, Y. Zhao, H. Huang, Y. Liu, Z. H. Kang, Bifunctional carbon dots as cocatalyst and reactor decorating an organic photocatalyst for H<sub>2</sub> production from water-splitting in an emulsion, *J. Mater. Chem. A* 11 (2023) 178–186.
- [8] Y.X. Li, W.Z. Zhang, H. Li, T.Y. Yang, S.Q. Peng, C. Kao, W.Y. Zhang, Ni-B coupled with borate-intercalated Ni(OH)<sub>2</sub> for efficient and stable electrocatalytic and photocatalytic hydrogen evolution under low alkalinity, *Chem. Eng. J.* 394 (2020), 124928.
- [9] T.T. Yao, X.R. An, H.X. Han, J.Q. Chen, C. Li, Photoelectrocatalytic materials for solar water splitting, *Adv. Energy Mater.* 8 (2018) 1800210.
- [10] X.C. Wang, K. Maeda, A. Thomas, K. Takanabe, G. Xin, J.M. Carlsson, K. Domen, M. Antonietti, A metal-free polymeric photocatalyst for hydrogen production from water under visible light, *Nat. Mater.* 8 (2008) 76–80.
- [11] Y.X. Li, M.F. Ji, Z.Y. Ma, L.H. Meng, R.C. He, S.Q. Peng, Hierarchically porous polymeric carbon nitride as a volume photocatalyst for efficient H<sub>2</sub> generation under strong irradiation, *Sol. RRL* 6 (2021) 2100823.
- [12] R.B. Guo, D.D. Zeng, Y. Xie, Y. Ling, D. Zhou, L.S. Jiang, W.Y. Jiao, J.S. Zhao, S. Q. Li, Carbon nitride quantum dots (CNQDs)/TiO<sub>2</sub> nanoparticle heterojunction photocatalysts for enhanced ultraviolet-visible-light-driven bisphenol a degradation and H<sub>2</sub> production, *Int. J. Hydrol. Energy* 45 (2020) 22534–22544.
- [13] Y.X. Li, R.C. He, P. Han, B.P. Hou, S.Q. Peng, C.Y. Ouyang, A new concept: volume photocatalysis for efficient H<sub>2</sub> generation - Using low polymeric carbon nitride as an example, *Appl. Catal. B-Environ.* 279 (2020), 119379.
- [14] A.V. Zhurenok, D.B. Vasilchenko, E.A. Kozlova, Comprehensive review on g-C<sub>3</sub>N<sub>4</sub>-based photocatalysts for the photocatalytic hydrogen production under visible light, *Int. J. Mol. Sci.* 24 (2023) 346.
- [15] F. He, M. Wang, S.Y. Shi, Y.R. Hou, M.Y. Lai, Z.X. Wang, S.Q. Peng, Y.X. Li, Confined synthesis of condensed π-conjugation C-PAN/MS-CN nanotubes for efficient photocatalytic H<sub>2</sub> evolution, *Chem. Commun.* 58 (2022) 4352–4355.
- [16] X.Y. Zou, Z.X. Sun, Y.H. Hu, g-C<sub>3</sub>N<sub>4</sub>-based photoelectrodes for photoelectrochemical water splitting: a review, *J. Mater. Chem. A* 8 (2020) 21474–21502.
- [17] Z.Y. Teng, Q.T. Zhang, H.B. Yang, K. Kato, W.J. Yang, Y.R. Lu, S.X. Liu, C.Y. Wang, A. Yamakata, C.L. Su, B. Liu, T. Ohno, Atomically dispersed antimony on carbon nitride for the artificial photosynthesis of hydrogen peroxide, *Nat. Catal.* 4 (2021) 374–384.
- [18] D. Liu, J.N. Shen, Y.Y. Xie, C.W. Qiu, Z.Z. Zhang, J.L. Long, H.X. Lin, X.X. Wang, Metallic Pt and PtO<sub>2</sub> dual-cocatalyst-loaded binary composite RGO-CN<sub>x</sub> for the

photocatalytic production of hydrogen and hydrogen peroxide, *ACS Sustain. Chem. Eng.* 9 (2021) 6380–6389.

[19] B. Tian, Y.Q. Wu, G.X. Lu, Metal-free plasmonic boron phosphide/graphitic carbon nitride with core-shell structure photocatalysts for overall water splitting, *Appl. Catal. B-Environ.* 280 (2021), 119410.

[20] X.X. Jia, J.W. Zhao, Y.J. Lv, X.L. Fu, Y.J. Jian, W.Q. Zhang, Y.Y. Wang, H.M. Sun, X. Wang, J.L. Long, P. Yang, Q. Gu, Z.W. Gao, Low-crystalline PdCu alloy on large-area ultrathin 2D carbon nitride nanosheets for efficient photocatalytic Suzuki coupling, *Appl. Catal. B-Environ.* 300 (2022), 120756.

[21] E.Q. Jin, Z. Lan, Q.H. Jiang, K.Y. Geng, G.S. Li, X.C. Wang, D.L. Jiang, 2D  $sp^2$  carbon-conjugated covalent organic frameworks for photocatalytic hydrogen production from water, *Chem. 5* (2019) 1632–1647.

[22] Y.R. Li, Y.Q. Wang, C.L. Dong, Y.C. Huang, J. Chen, Z. Zhang, F.Q. Meng, Q. H. Zhang, Y. Huangfu, D.M. Zhao, L. Gu, S.H. Shen, Single-atom nickel terminating  $sp^2$  and  $sp^3$  nitride in polymeric carbon nitride for visible-light photocatalytic overall water splitting, *Chem. Sci.* 12 (2021) 3633–3643.

[23] S.Q. Peng, C. Gan, Y. Yang, S.F. Ji, Y.X. Li, Low Temperature and controllable formation of oxygen vacancy  $SrTiO_{3-\delta}$  by loading Pt for enhanced photocatalytic hydrogen evolution, *Energy Technol.* 6 (2018) 2166–2171.

[24] Y.Q. Wang, Y. Xie, S.H. Yu, K. Yang, Y. Shao, L.X. Zou, B.X. Zhao, Z.L. Wang, Y. Ling, Y. Chen, Ni doping in unit cell of BiOBr to increase dipole moment and induce spin polarization for promoting  $CO_2$  photoreduction via enhanced build-in electric field, *Appl. Catal. B-Environ.* 327 (2023), 122420.

[25] S.Q. Peng, Y. Cao, F.X. Zhou, Z.D. Xu, Y.X. Li, CoP decorated with  $Co_3O_4$  as a cocatalyst for enhanced photocatalytic hydrogen evolution via dye sensitization, *Appl. Surf. Sci.* 487 (2019) 315–321.

[26] D.B. Wu, F. He, Y.H. Dai, Y. Xie, Y. Ling, L.J. Liu, J.S. Zhao, H. Ye, Y. Hou, A heterostructured ZnAl-LDH@ZIF-8 hybrid as a bifunctional photocatalyst/adsorbent for  $CO_2$  reduction under visible light irradiation, *Chem. Eng. J.* 446 (2022), 137003.

[27] Y.X. Li, Y.L. Hou, Q.Y. Fu, S.Q. Peng, Y.H. Hu, Oriented growth of  $ZnIn_2S_4/In(OH)_3$  heterojunction by a facile hydrothermal transformation for efficient photocatalytic  $H_2$  production, *Appl. Catal. B-Environ.* 206 (2017) 726–733.

[28] Y.X. Li, P. Han, Y.L. Hou, S.Q. Peng, X.J. Kuang, Oriented  $Zn_mIn_2S_{m+3}/In_2S_3$  heterojunction with hierarchical structure for efficient photocatalytic hydrogen evolution, *Appl. Catal. B-Environ.* 244 (2019) 604–611.

[29] J. Liu, M.Y. Wu, H. Ye, Y. Xie, Y.C. Ma, L.J. Liu, Strong interaction between sulfur sites and oxygen vacancies in Z-scheme  $ZnIn_2S_4/TiO_{2-x}$  heterojunction for improved photocatalytic hydrogen yield and stability, *Chem. Eng. J.* 455 (2023), 140722.

[30] Z. Liang, L.L. Yin, H. Yin, Z.Y. Yin, Y.P. Du, Rare earth element based single-atom catalysts: synthesis, characterization and applications in photo/electro-catalytic reactions, *Nanoscale Horiz.* 7 (2022) 31–40.

[31] M. Ismael, Environmental remediation and sustainable energy generation via photocatalytic technology using rare earth metals modified g-C<sub>3</sub>N<sub>4</sub>: A review, *J. Alloy. Compd.* 931 (2023), 167469.

[32] D.D. Zeng, F. He, Y.X. Li, Construction of terbium oxide/polymer carbon nitride heterojunction for boosting photocatalytic overall water splitting without cocatalyst, *Appl. Catal. A-Gen.* 650 (2023), 118986.

[33] C. Liu, Q.F. Zhang, Z.G. Zou, Recent advances in designing  $ZnIn_2S_4$ -based heterostructured photocatalysts for hydrogen evolution, *J. Mater. Sci. Technol.* 139 (2023) 167–188.

[34] Y.X. Li, S.Q. Li, L.H. Meng, S.Q. Peng, Synthesis of oriented J type  $ZnIn_2S_4@CdIn_2S_4$  heterojunction by controllable cation exchange for enhancing photocatalytic hydrogen evolution, *J. Colloid Interface Sci.* <https://doi.org/10.1016/j.jcis.2023.06.185>.

[35] J.Y. Yan, C.H. Wang, H. Ma, Y.Y. Li, Y.C. Liu, N. Suzuki, C. Terashima, A. Fujishima, X.T. Zhang, Photothermal synergic enhancement of direct Z-scheme behavior of  $Bi_4TaO_8Cl/W_{18}O_{49}$  heterostructure for  $CO_2$  reduction, *Appl. Catal. B-Environ.* 268 (2020), 118401.

[36] Z.H. Mei, G.H. Wang, S.D. Yan, J. Wang, Rapid microwave-assisted synthesis of 2D/1D  $ZnIn_2S_4/TiO_2$  S-scheme heterojunction for catalyzing photocatalytic hydrogen evolution, *Acta Phys. -Chim. Sin.* 37 (6) (2021) 2009097–2009100.

[37] S.C. Liu, K. Wang, M.X. Yang, Z.L. Jin, Rationally designed  $Mn_{0.2}Cd_{0.8}S@CoAl LDH$  S-scheme heterojunction for efficient photocatalytic hydrogen production, *Acta Phys. -Chim. Sin.* 38 (7) (2021), 2109023–2109032.

[38] A. Han, X.J. Wang, K. Tang, Z.D. Zhang, C.L. Ye, K.J. Kong, H.B. Hu, L.R. Zheng, P. Jiang, C.X. Zhao, Q. Zhang, D.S. Wang, Y.D. Li, An adjacent atomic platinum site enables single-atom iron with high oxygen reduction reaction performance, *Angew. Chem. Int. Ed.* 60 (2021) 2–12.

[39] T. Ma, H. Cao, S. Li, S. Cao, Z. Zhao, Z. Wu, R. Yan, C. Yang, Y. Wang, P.A. van Aken, L. Qiu, Y.G. Wang, C. Cheng, Crystalline lattice-confined atomic Pt in metal carbides to match electronic structures and hydrogen evolution behaviors of platinum, *Adv. Mater.* 34 (2022) 2206368.

[40] G.G. Zhang, Z.A. Lan, L.H. Lin, S. Lin, X.C. Wang, Overall water splitting by Pt/g-C<sub>3</sub>N<sub>4</sub> photocatalysts without using sacrificial agents, *Chem. Sci.* 7 (2016) 3062–3066.

[41] Y.X. Li, H. Wang, S.Q. Peng, Tunable photodeposition of MoS<sub>2</sub> onto a composite of reduced graphene oxide and CdS for synergic photocatalytic hydrogen generation, *J. Phys. Chem. C.* 118 (2014) 19842–19848.

[42] L.W. Zhang, R. Long, Y.M. Zhang, D.L. Duan, Y.J. Xiong, Y.J. Zhang, Y.P. Bi, Direct observation of dynamic bond evolution in single-atom Pt/C<sub>3</sub>N<sub>4</sub> catalysts, *Angew. Chem. Int. Ed.* 59 (2020) 6224–6229.

[43] P. Zhang, L. Li, J. Zhao, H. Wang, X.D. Zhang, Y. Xie, Elemental doping boosts charge-transfer excitonic states in polymeric photocatalysts for selective oxidation reaction, *Precis. Chem.* 1 (2023) 40–48.

[44] B.C. Zhu, P.F. Xia, W.K. Ho, J.G. Yu, Isoelectric point and adsorption activity of porous g-C<sub>3</sub>N<sub>4</sub>, *Appl. Surf. Sci.* 344 (2015) 188–195.

[45] S. Kitaoka, N. Kawashima, K. Maeda, T. Kuno, Y. Noguchi, Design of mold materials for encapsulating semiconductors using epoxy molding compounds, *Mater. Sci. Forum* 561–565 (2007) 539–542.

[46] Q.F. Wang, L. Zhang, L.Y. Qiu, J.Q. Sun, J.C. Shen, Fabrication and electrochemical investigation of layer-by-layer deposited titanium phosphate/prussian blue composite films, *Langmuir* 23 (2007) 6084–6090.

[47] Z.H. Zhang, J.S. Tian, Y.B. Lu, S.Z. Yang, D. Jiang, W.X. Huang, Y.X. Li, J.Y. Hong, A.S. Hoffman, S.R. Bare, M.H. Engelhard, A.K. Datye, Y. Wang, Memory-dictated dynamics of single-atom Pt on CeO<sub>2</sub> for CO oxidation, *Nat. Commun.* 14 (2023) 2664.

[48] W. Zhang, W.J. Chen, Q. Xiao, L. Yu, C.Q. Huang, G.X. Lu, A.W. Morawski, Y. Yu, Nitrogen-coordinated metallic cobalt disulfide self-encapsulated in graphitic carbon for electrochemical water oxidation, *Appl. Catal. B-Environ.* 268 (2020), 118449.

[49] B. Han, Y.L. Guo, Y.K. Huang, W. Xi, J. Xu, J. Luo, H.F. Qi, Y.J. Ren, X.Y. Liu, B. T. Qiao, T. Zhang, Strong metal-support interactions between Pt single atoms and TiO<sub>2</sub>, *Angew. Chem. Int. Ed.* 59 (2020) 11824–11829.

[50] R. Lang, X.R. Du, Y.K. Huang, X.Z. Jiang, Q. Zhang, Y.L. Guo, K.P. Liu, B.T. Qiao, A. Q. Wang, T. Zhang, Single-atom catalysts based on the metal–oxide interaction, *Chem. Rev.* 120 (2020) 11986–12043.

[51] J. Liu, C. Wang, W.B. Yu, H. Zhao, Z.Y. Hu, F. Liu, T. Hasan, Y. Li, G. Van Tendeloo, C. Li, B.L. Su, Bioinspired noncyclic transfer pathway electron donors for unprecedented hydrogen production, *CCS Chem.* 5 (2023) 1470–1482.

[52] S. Bai, C.M. Wang, M.S. Deng, M. Gong, Y. Bai, J. Jiang, Y.J. Xiong, Surface polarization matters: enhancing the hydrogen-evolution reaction by shrinking Pt shells in Pt-Pd-graphene stack structures, *Angew. Chem. Int. Ed.* 53 (2014) 12120–12124.

[53] J. Liu, Y. Liu, N.Y. Liu, Y.Z. Han, X. Zhang, H. Huang, Y. Lifshitz, S.Y. Lee, J. Zhong, Z.H. Kang, Metal-free efficient photocatalyst for stable visible watersplitting via a two-electron path way, *science* 347 (2015) 6225.

[54] J.P. Sun, J.B. Weng, T. Lin, L.P. Ma, Preparation and Photophysical Properties of Poly(2-methoxy-5-octyloxy)-p-phenylene Vinylene/Tb<sub>4</sub>O<sub>7</sub> Nanocomposites, *Acta Chim. Sin.* 68 (2010) 1337–1342.

[55] J.H. Kim, J.A. Hong, D.G. Kwon, J. Seo, Y. Park, Energy level alignment in polymer organic solar cells at donor-acceptor planar junction formed by electrospray vacuum deposition, *Appl. Phys. Lett.* 104 (2014), 163303.

[56] T.G. Castner, Criterion for the size of the scaling regime for the metal-insulator transition of doped semiconductors, *Phys. Rev. B* 67 (2003), 193202.

[57] L. Yang, R. Grzeschik, P. Jiang, L.F. Yu, C.J. Hu, A.X. Du, S. Schlücker, W. Xie, Tuning the electronic properties of platinum in hybrid-nanoparticle assemblies for use in hydrogen evolution reaction, *Angew. Chem. Int. Ed.* 62 (2023), e202301065.

[58] Y. Yu, D. Lee, B. Jeong, The dependence of the work function of Pt (111) on surface carbon investigated with near ambient pressure X-ray photoelectron spectroscopy, *Appl. Surf. Sci.* 607 (2023), 155005.